



Review

# Imaging Metabolically Active Fat: A Literature Review and Mechanistic Insights

Joseph Frankl <sup>1</sup>, Amber Sherwood <sup>1</sup>, Deborah J. Clegg <sup>2</sup>, Philipp E. Scherer <sup>3</sup> and Orhan K. Öz <sup>1,\*</sup>

<sup>1</sup> Department of Radiology, University of Texas Southwestern Medical Center, 5323 Harry Hines Blvd, Dallas, TX 75390-8542, USA; joseph.frankl@utsouthwestern.edu (J.F.); amber.sherwood@utsouthwestern.edu (A.S.)

<sup>2</sup> College of Nursing and Health Professions, Drexel University, 10th Floor, Room 1092, 1601 Cherry Street, Mail Stop 10501, Philadelphia, PA 19102, USA; debclegg@outlook.com

<sup>3</sup> Department of Internal Medicine, Touchstone Diabetes Center, University of Texas Southwestern Medical Center, 5323 Harry Hines Blvd, Dallas, TX 75390-8542, USA; philipp.scherer@utsouthwestern.edu

\* Correspondence: orhan.oz@utsouthwestern.edu

Received: 6 October 2019; Accepted: 1 November 2019; Published: 5 November 2019



**Abstract:** Currently, obesity is one of the leading causes death in the world. Shortly before 2000, researchers began describing metabolically active adipose tissue on cancer-surveillance <sup>18</sup>F-fluorodeoxyglucose (FDG) positron emission tomography/computed tomography (PET/CT) in adult humans. This tissue generates heat through mitochondrial uncoupling and functions similar to classical brown and beige adipose tissue in mice. Despite extensive research, human brown/beige fat's role in resistance to obesity in humans has not yet been fully delineated. FDG uptake is the de facto gold standard imaging technique when studying brown adipose tissue, although it has not been rigorously compared to other techniques. We, therefore, present a concise review of established and emerging methods to image brown adipose tissue activity in humans. Reviewed modalities include anatomic imaging with CT and magnetic resonance imaging (MRI); molecular imaging with FDG, fatty acids, and acetate; and emerging techniques. FDG-PET/CT is the most commonly used modality because of its widespread use in cancer imaging, but there are mechanistic reasons to believe other radiotracers may be more sensitive and accurate at detecting brown adipose tissue activity. Radiation-free modalities may help the longitudinal study of brown adipose tissue activity in the future.

**Keywords:** Brown adipose tissue; FDG; PET/CT; SPECT; fatty acids; acetate; carbon-13; MSOT; obesity

## 1. Introduction

Obesity is caused by chronic excess of calories consumed relative to calories burned. Development of obesity is often accompanied by metabolic dysfunction including dyslipidemia and diabetes. Other associated diseases include cancer, cardiovascular disease, osteoarthritis, and nonalcoholic fatty liver disease [1]. Improving treatment of obesity and obesity-related conditions is a priority in the developed world. In the United States of America alone, obesity is estimated to contribute to over 175,000 excess deaths per year [2]. Healthcare costs attributable to obesity may now exceed \$150 billion annually in the United States [3]. Major professional society guidelines recommend pharmacotherapy as a treatment option for obesity (body mass index [BMI] >30 kg/m<sup>2</sup>) and overweight with a BMI >27 kg/m<sup>2</sup> and associated comorbidities such as type 2 diabetes, obstructive sleep apnea, or hypertension [4,5]. A recent systematic review found that currently approved medications have demonstrated efficacy between 40–75% for reducing weight by 5% over 52 weeks compared to 23% for placebo [6]. Some of the most efficacious medications are however also associated with treatment

discontinuation because of adverse effects [6]. There remains an unmet need for efficacious and tolerable medications for the treatment of obesity and prevention of obesity-related complications.

One potential target for medical therapies aimed at reducing obesity and preventing associated metabolic dysfunction is metabolically active fat tissue. Human infants have classical interscapular brown adipose tissue that is of myogenic origin and is analogous to the primary thermogenic fat depots in mice and other small mammals [7]. This tissue is thought to recede quickly with age [7,8]. However, a significant proportion of human adults have metabolically active fat tissue in the supraclavicular and cervical areas as detected by  $^{18}\text{F}$ -fluorodeoxyglucose (FDG) positron emission tomography (PET) following cold exposure [9–11]. Unlike classical brown adipose tissue (BAT) with its relatively homogenous collection of multilocular adipocytes, metabolically active fat tissue in adults has multilocular adipocytes of adipogenic precursor origin interspersed among typical, unilocular white adipocytes [12]. Like adipocytes in classical BAT, multilocular adipocytes in this adult tissue (which goes by multiple terms including “beige” and “brite” adipose tissue, but will be called inducible BAT [iBAT] in this review, consistent with a National Institutes of Health [NIH] convened expert panel’s preferred terminology) generate heat and consume energy stores through mitochondrial uncoupling via *Ucp1* [12,13]. Its presence is thought to decrease with age, obesity, and has been shown to be usually lower in men than women in several studies [14–16], although in clinical practice there is wide variation. Figure 1 summarizes the physiological differences between thermogenic BAT and lipid-storing WAT.

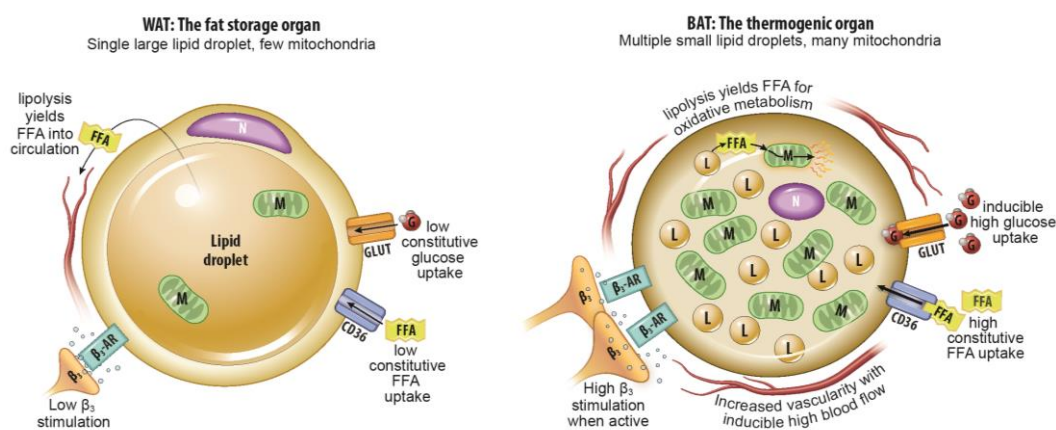


**Figure 1.** Summary of major physiological differences between white adipose tissue (WAT) and brown adipose tissue (BAT). A summary of major physiological differences relevant to imaging between WAT and BAT. FFA: free fatty acid, N: nucleus, M: mitochondria,  $\beta_3$ -AR: beta-3 adrenergic receptor, G: glucose, L: lipid droplet, CD36: cluster of differentiation 36/fatty acid translocase, GLUT: glucose transporter.

Most analyses of inducible BAT in human adults have used FDG-PET. However, this modality has several limitations for the purpose of identifying and quantifying iBAT: it does not detect inactive iBAT as judged by small animal studies assessed by other imaging modalities. Furthermore, it relies on glucose uptake, whereas iBAT generates most of its energy from stored triglycerides. Also, FDG-PET criteria for identifying iBAT vary between studies [13,17,18]. Molecular imaging strategies that probe oxidative metabolism or free fatty acid uptake may therefore be more sensitive to iBAT presence and activity than FDG-PET. Application of any radiotracer-based molecular imaging study in longitudinal studies with human subjects must take into account radiation dose. Magnetic resonance imaging (MRI) allows for repeated scans without radiation and can take advantage of the known difference in typical fat fraction and mitochondrial density between iBAT and white adipose tissue (WAT) [19]. However, intrasubject variability and iBAT cellular composition changes over time may limit the utility of current MRI methods [20,21]. Emerging techniques with multispectral optoacoustic tomography and  $^{13}\text{C}$ -MRI may eventually be used more often in research of iBAT. However, the optimal imaging

strategy for detection and longitudinal study of iBAT in humans remains to be determined. In this review, we describe different techniques, their application, limitations, and areas for further research.

## 2. Anatomic Imaging

### 2.1. Computed Tomography

Computed tomography (CT) utilizes x-rays to generate a 3-dimensional dataset of tissue attenuation values that can be reconstructed into images in multiple planes. Different x-ray attenuation values of tissues form the basis of CT contrast. CT images have high resolution. iBAT is most often encountered in humans on CTs obtained during PET-CT studies in cancer patients. Although CT does not directly provide any functional data, radiodensity, which in the case of adipose tissue is largely determined by the ratio of fat to water, can be compared between different locations and quantitated using the Hounsfield scale [22–24]. The multilocular Ucp1-rich adipocytes have a higher fraction of water than their WAT counterparts and thus should be more radiodense [22,25]. Indeed, Prodhomme and colleagues found adipose tissue identified as metabolically active with FDG-PET has higher mean Hounsfield units (HU) than FDG non-avid WAT ( $-32.6 \pm 26$  vs.  $-99.6 \pm 18.8$  HU) [16]. HUs increase further with activation and utilization of lipid by BAT in rodents and humans [26–28]. Obese individuals have lower mean Hus in typical location of iBAT as in the supraclavicular region consistent with greater lipid content, and mean HU increases with weight loss [29]. In addition to supraclavicular depots, relatively high-attenuation fat depots in cervical, axillary, mediastinal, and intraabdominal locations may be iBAT [10,30,31]. CT demonstrates the known greater vascular density in BAT compared to WAT in our experience (Figure 2) [32].

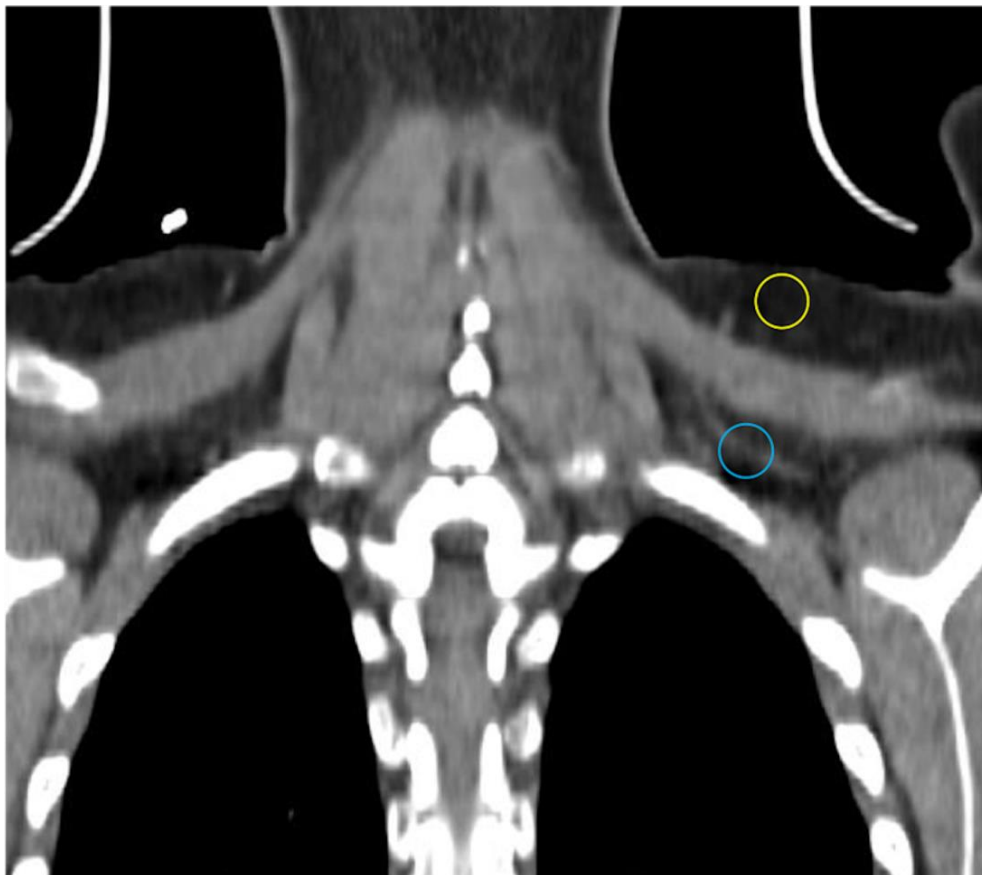


**Figure 2.** CT showing different density and vascularity of BAT versus WAT. Subcutaneous WAT with a darker appearance on conventional display and fewer vessels (yellow circle) compared with BAT (blue circle).

## 2.2. Magnetic Resonance Imaging

Conventional proton MRI takes advantage of the small magnetic field produced by hydrogen atoms. Broadly, the MRI scanner produces a strong magnetic field that causes hydrogen atoms to align; so there is a small net magnetization aligned with the external magnetic field. Radiofrequency pulses flip hydrogen atoms out of alignment. The rate at which hydrogen atoms return to alignment with the external magnetic field is termed T1. When the aligned magnetic fields of hydrogen atoms transverse the external magnetic field, the rate at which they leave alignment with the transverse plane is termed T2. T1- and T2-weighted images are the most common MR images [33]. Additional MR acquisitions and image processing techniques can produce images that reflect the fat/water ratio and mitochondrial density, which both may be helpful in BAT research [19].

Stojanovska and colleagues showed water-fat imaging distinguishes ex vivo samples of BAT, WAT, and mixed BAT/WAT from each other. Specifically, the proton density fat fraction as a percent was significantly lower in BAT compared to other samples [34]. As mentioned above, this is because BAT has less lipid deposits than WAT. A similar technique successfully discriminated BAT from WAT in rodents and additionally correlated the two different depots with specific CT HU ranges [35]. Dixon-based MRI, a technique for generating fat and water images, and several investigational water-fat algorithms have differentiated iBAT from WAT in human subjects [19,36–39]. Results were confirmed by FDG uptake detected separately on PET/CT or in the same scan via PET/MRI [19,38,40]. At thermoneutral conditions, the MR fat fraction differentiates iBAT from WAT with greater sensitivity than FDG-PET/CT (Figure 3) [19,41,42]. Cold stimulation accentuates the fat-fraction difference between BAT and WAT, as even short-duration cold exposure induces lipid utilization by Ucp1-rich adipocytes [20,39,40]. A limitation of fat-fraction MR in this setting is variability between subjects in the optimal cutoff value to distinguish BAT from WAT [21]. Romu and colleagues showed calibrating fat images based on the T2\*-derived fat content of WAT to form relative fat content images can identify BAT in rats and may avoid the pitfall of inter-subject variability by using an internal control [35].

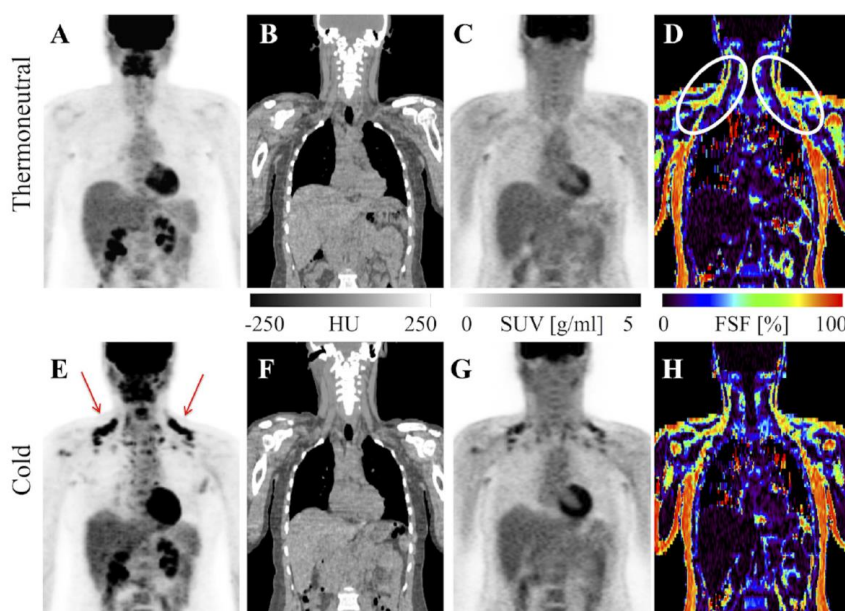


**Figure 3.** MRI vs. FDG-PET/CT in detection of BAT. FDG-PET/CT and MRI of a healthy BAT-positive research subject. FDG uptake is visible in supraclavicular BAT with cold exposure on the PET maximum intensity projection (MIP; E, red arrows) and absent from the thermoneutral PET MIP (A). CT shows adipose tissue in the same region (B,F) and PET shows increased standardized uptake value there after exposure to cold (C,G). MRI-derived fat signal fraction from the same subject shows adipose tissue with relatively low levels of fat (white ovals) in the same region at thermoneutral and cold conditions (D,H). Image reproduced with permission from reference 41.

$R2^*$  and  $T2^*$  images also differentiate iBAT from WAT.  $T2^*$  is a time constant generated from the signal decay immediately following the initial excitation pulse and  $R2^*$  is the inverse of  $T2^*$  [43]. These parameters are influenced by the iron content of mitochondria, which are present at high density in iBAT [44,45]. Greater blood flow to BAT/iBAT compared to WAT may also contribute to  $R2^*$  and  $T2^*$  differentiation [41]. Lundström and colleagues showed  $R2^*$  maps have a high degree of overlap with MR fat fraction maps of iBAT [37]. However, unlike fat-fraction,  $R2^*$  does not change significantly with acute cold exposure likely because mitochondrial density does not change [41].

There are several emerging MR-based techniques. Functional MRI may be applied to detect changes in blood flow in activated iBAT in future research although few investigators have used it in BAT research thus far [46]. Blood oxygenation level dependent functional MRI signal increased in iBAT upon cold exposure in one small ( $n = 3$ ) study with adult humans (Figure 4) [47]. MR thermometry is an emerging technique that measures tissue temperature and may provide an additional measure of iBAT activity [40].

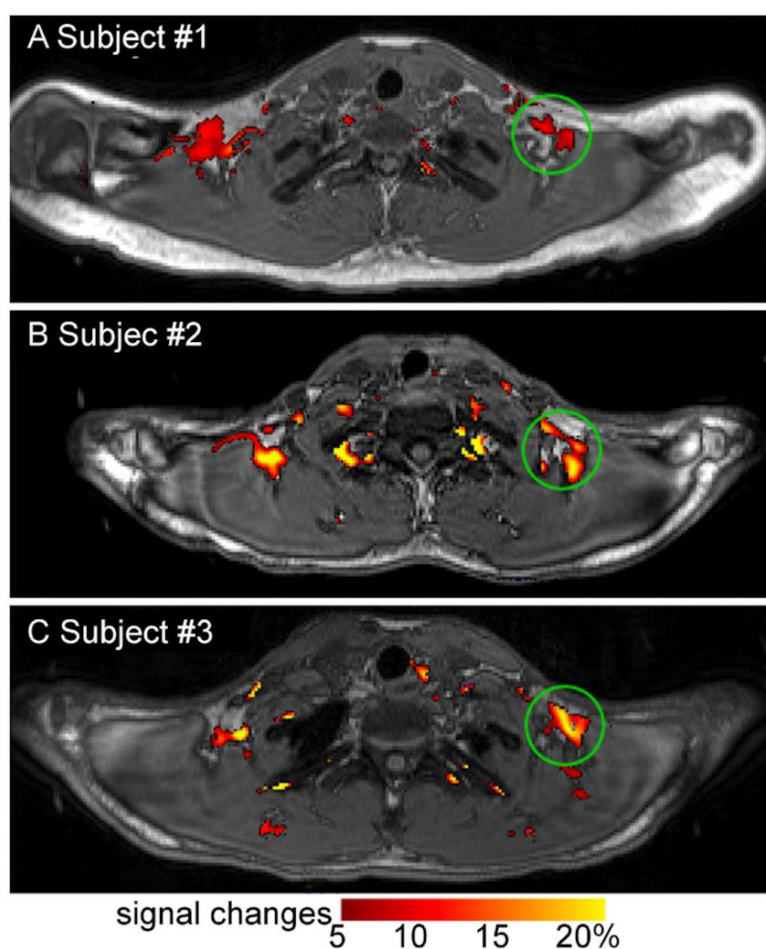


**Figure 4.** Change in blood oxygen level dependent MRI signal in human BAT with cold exposure. Change in blood oxygen level dependent MRI signal in supraclavicular BAT with cold exposure (13–16 °C) in healthy human research subjects. Images A, B, and C are representative images of 3 subjects. Image reproduced with permission from reference 47.

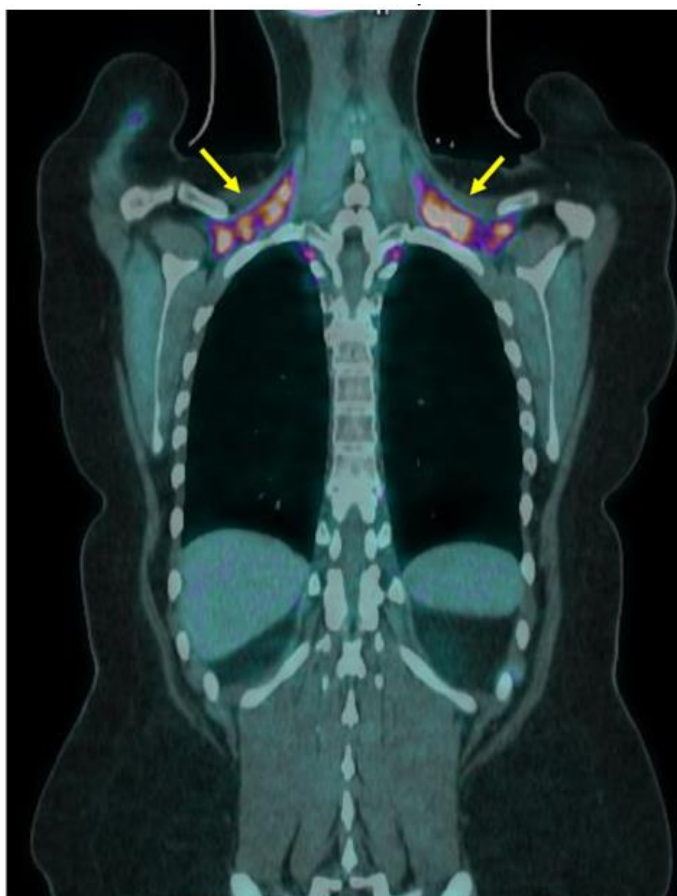
### 3. Molecular Imaging with Radiotracers

#### 3.1. $^{18}\text{F}$ -Fluorodeoxyglucose-PET

FDG-PET/CT is the de facto gold standard imaging study in BAT research [13]. However, a mechanistic understanding of FDG uptake and BAT physiology challenges FDG-PET/CT's current

role. FDG is transported into cells via glucose transporters. It is phosphorylated, like glucose, to FDG-6-phosphate, but does not undergo further metabolism [48]. Trapped FDG-6-phosphate is detected in locations with greater glucose uptake and utilization. BAT's primary source of energy is the intracellular triglyceride pool [49]. FDG uptake occurs as metabolically active adipocytes replenish their lipid pools, but this is a downstream event from BAT thermogenesis. Some amount of glucose uptake also occurs via acute  $\beta_3$ -adrenergic receptor stimulation [50]. Nevertheless, FDG-PET/CT is an important technique in BAT research from a historical perspective and remains the most widely used imaging study in this setting. Large retrospective reviews of atypical supraclavicular FDG uptake in oncology patients were among the first indication of iBAT prevalence in adult humans [51,52]. Dedicated BAT research protocols have since used FDG-PET/CT to establish much of the current BAT literature. Advantages of FDG include its availability and the high number of clinical scans performed at large oncology centers, which generate databases amenable to BAT research.

The rate of iBAT detected on a single FDG-PET/CT scan in large oncology cohorts is between 5–10% [14,16,53]. However, rate of detection rises substantially with repeated scanning or cold stimulation, although estimated prevalence varies widely between 20–100% [53–55]. Figure 5 shows an example of a patient with variably detectable iBAT. Indeed, seasonal changes in temperature impact iBAT prevalence estimates, limiting the utility of retrospective cohort studies [31]. Female gender and younger age have been associated with increased iBAT prevalence in large retrospective studies [15,56]. Lower adiposity, particularly visceral adiposity, is also associated with increased iBAT detection on FDG-PET/CT [15,57]. However, the lack of sensitivity to inactive BAT presents a problem to clinical BAT research as the most relevant subjects are obese and metabolically unhealthy.



A

Figure 5. Cont.

**B**

**Figure 5.** Example of variable iBAT uptake on FDG-PET/CT. FDG-PET/CT in a woman in her 20s showing marked BAT uptake in (A) November (yellow arrows) and no detectable BAT FDG uptake on a scan (B) 6 months later.

Prospective studies often use cooling protocols to induce iBAT activation. Leitner and colleagues showed a 20 min cold exposure is sufficient to activate iBAT in healthy adult volunteers [58]. In their study, 3 h of rewarming after cold exposure decreased FDG uptake by iBAT to near baseline [58]. Indeed, iBAT is so temperature sensitive a NIH expert panel recommends reporting outdoor temperature, season, and geographic location in any FDG-PET/CT study of iBAT [13]. Despite the strong association with cooler temperatures, we routinely see active iBAT on warm days in our large oncology practice where the uptake room is held at a constant temperature warm enough to prevent shivering. Figure 6 shows examples of the wide variation of uptake in clinical patients.

The above-mentioned NIH panel released the first guidelines on reporting FDG-PET findings in BAT research, named the Brown Adipose Reporting Criteria in Imaging Studies (BARCIST 1.0). Prior to that, criteria to identify metabolically active fat tissue varied greatly [18]. Their recommendations were to label regions with HUs between  $-190$  and  $-10$  and standardized uptake values (SUV) of  $1.2/(\text{lean body mass})/(\text{body mass})$  as brown fat. Additional recommendations include reporting subject body weight, height, and BMI; reporting liver and descending aorta SUV to establish background activity; having subjects fast 6 h prior, refrain from eating fatty meals 24 h prior, and not consume caffeine or capsinoids within 48 h of scanning; and excluding smokers and individuals on sympathomimetics and sympatholytics [13].

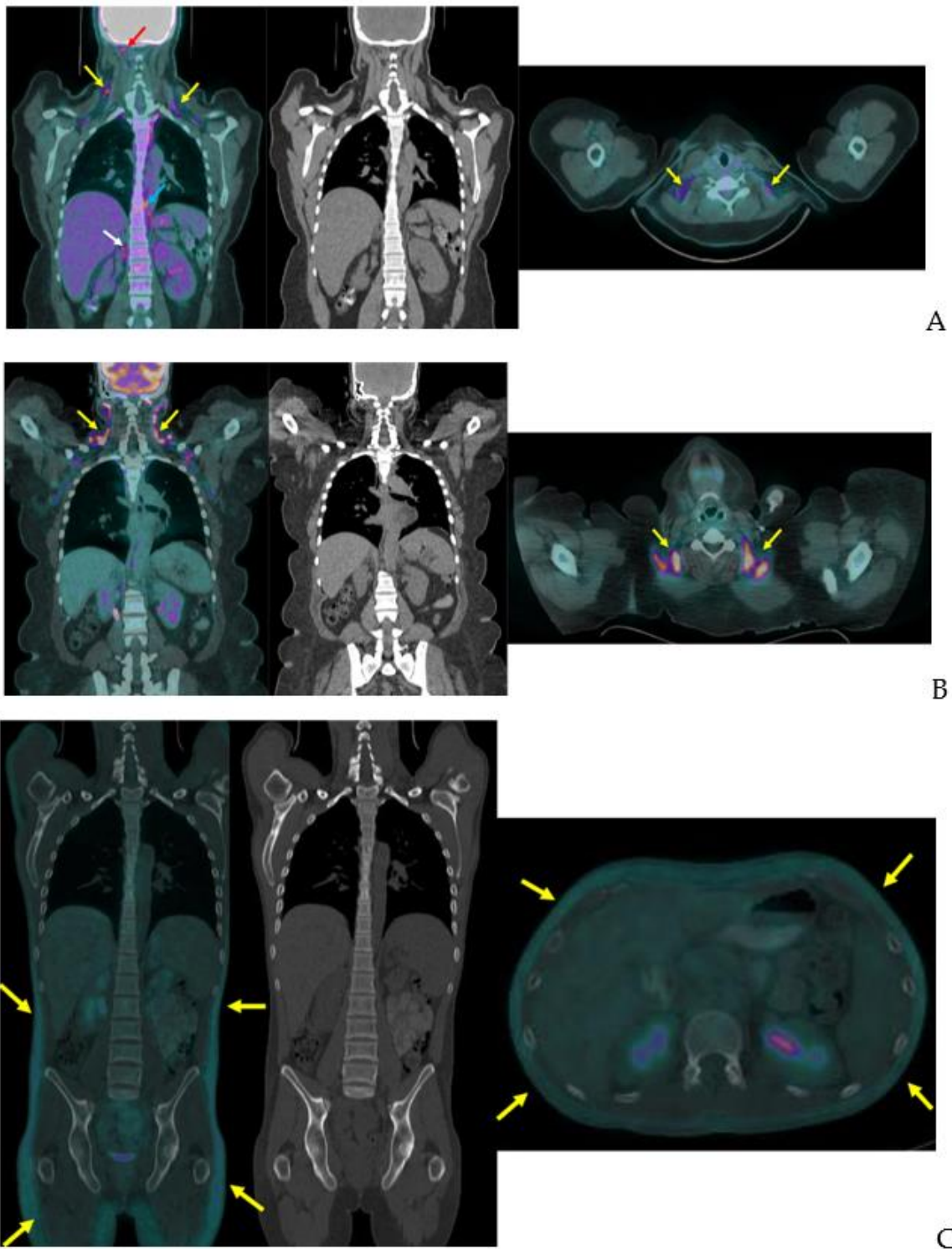
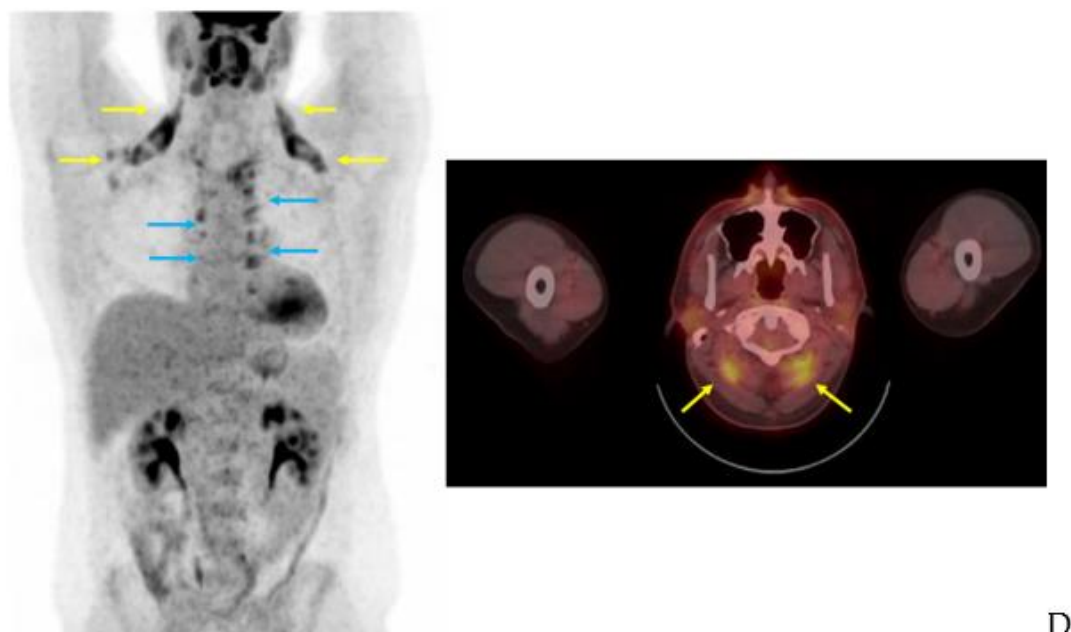


Figure 6. Cont.



**Figure 6.** Variation of BAT FDG uptake in clinical patients. Fused coronal FDG-PET/CT, coronal CT, and fused axial FDG-PET/CT (A–C). (A) BAT FDG uptake in a woman with normal BMI. Note supraclavicular (yellow arrows), skull base (red arrow), paraesophageal (blue arrow), and perinephric (white arrow) uptake. (B) Supraclavicular BAT in an obese woman (yellow arrows). (C) Diffuse FDG uptake in subcutaneous WAT in a male patient (yellow arrows). (D) A male patient with extensive supraclavicular FDG uptake extending into the upper neck (yellow arrows) and paravertebral BAT activity (blue arrows).

### 3.2. $^{18}\text{F}$ -Fluoro-6-Thia-Heptadecanoic Acid (FTHA) PET

FTHA is a fatty acid probe that is transported into cells by fatty-acid transport protein gets trapped in the mitochondria after commitment to the mitochondrial fatty acid oxidation pathway [59]. It was initially developed to assess oxygenation of myocardium [59]. It has since been used by several groups to assess fatty acid uptake by BAT (Figure 7). Labbé and colleagues showed FTHA localizes to BAT as FDG does with cold stimulation in rodents [49,60]. FTHA actually identified additional periaortic and cervical BAT depots FDG did not manage to pinpoint [49]. Ouellet showed dynamic FTHA uptake over 30 min increases with in adult human iBAT with cold exposure using Patlak graphical analysis [28]. Dadson and colleagues found dynamic FTHA uptake over 15 min increased in iBAT after bariatric surgery in a cohort of morbidly obese women using graphical analysis with concomitant increase in CT radiodensity, indicating lower intracellular iBAT lipid stores [29].

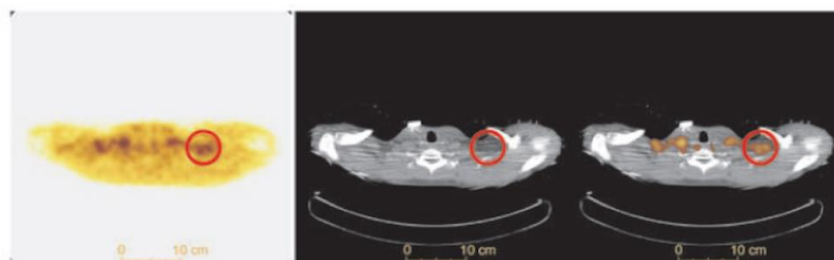


**Figure 7.** BAT FTHA uptake in a healthy human subject. Transverse FTHA-PET (left panel), CT (middle panel) and fused PET/CT (right panel) in a healthy subject after 1 h of cold exposure. Supraclavicular BAT is shown in the red circle. Image reproduced with permission from reference 28.

### 3.3. $^{123}\text{I}$ -Beta-Methyl-Iodophenyl-Pentadecanoic Acid (BMIPP) Single-Photon Emission Computed Tomography (SPECT)/CT

BMIPP is a fatty acid tracer routinely used for cardiac SPECT/CT in Japan [61]. It is transported into the cell by CD36 and trapped during incomplete  $\beta$  oxidation [62,63]. Although developed in the United States, it is not approved for clinical use by the Food and Drug Administration. Research with BMIPP likely requires on-site synthesis. However, synthesis does not require a cyclotron as the long (13 h) half-life of  $^{123}\text{I}$  makes it suitable for transport [64]. Additionally,  $^{125}\text{I}$ -labeled BMIPP produces high-resolution images on preclinical scanners and has a half-life of nearly 60 days [65]. In our hands, BMIPP identified BAT depots missed by FDG-PET/CT in mice (Figure 8) [30]. Additionally, BMIPP-SPECT/CT has a much more favorable signal-to-noise compared to FTHA-PET/CT [30]. We believe it is a measure of flux through the triglyceride pool.

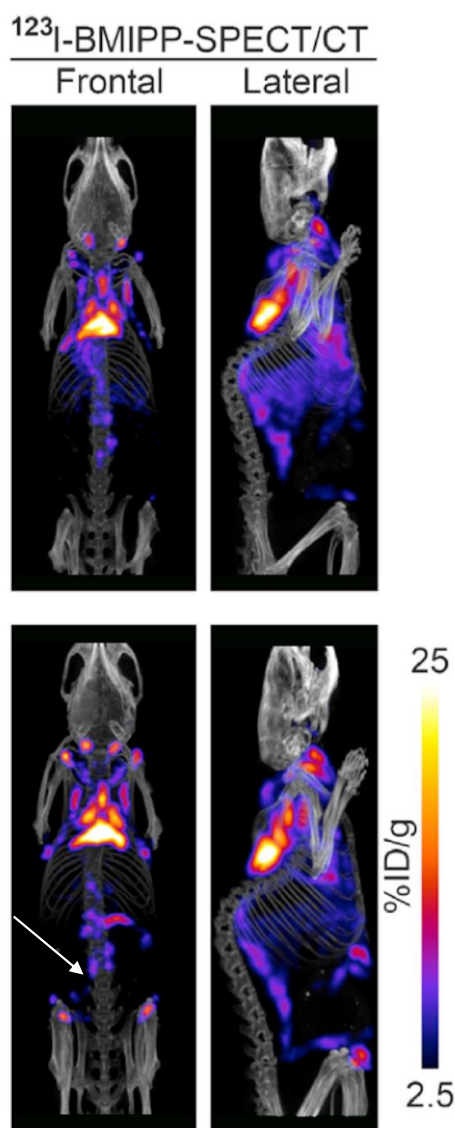


**Figure 8.** BMIPP-SPECT/CT with and without beta-adrenergic stimulation. BMIPP-SPECT/CT scanning for the patterns of fatty acid uptake in the metabolically active fat tissues of adult mice at room temperature after 7 days of vehicle treatment (top) or 7 days of treatment with the  $\beta_3$ -adrenergic agonist CL-316243 (bottom row). Treatment increased uptake in classical interscapular BAT cervical depots, and inducible anterior abdominal subcutaneous (arrow) and inguinal metabolically active fat tissue. Image reproduced with permission from reference 30.

### 3.4. $^{11}\text{C}$ -Acetate-PET

Acetate is transported into cells via monocarboxylate transporters and converted to acetyl-CoA by acyl-CoA synthetases prior to catabolism in the citric acid cycle or use in biosynthetic reactions [66,67]. Clinically,  $^{11}\text{C}$ -acetate is used to measure myocardial oxygen consumption and malignant lipogenesis by slow-growing, FDG non-avid tumors [68–72]. A fitted monoexponential function ( $K_{\text{mono}}$ ) of clearance beginning after blood pool stabilization is used in cardiac studies to estimate oxidative metabolism via the citric acid cycle [69,70].  $^{11}\text{C}$ -acetate's use in cancer imaging is similar to FDG-PET with  $\text{SUV}_{\text{max}}$  and  $\text{SUV}_{\text{mean}}$  more often followed [71,72]. These values reflect incorporation of the radiotracer into fatty acids. Wider use is limited by the need for an on-site cyclotron because of carbon-11's short half-life (~20.38 min) [73].

$^{11}\text{C}$ -acetate's ability to assess oxidative metabolism is utilized in study of metabolically active fat tissue in rodents and humans [27,28,60,74]. Clearance after blood pool stabilization at 2–4 min through up to approximately 17.5 min after radiotracer injection is due to conversion into  $\text{CO}_2$  in the citric acid cycle [68]. Acute and chronic cold exposure increase  $^{11}\text{C}$ -acetate  $K_{\text{mono}}$  by classical BAT depots in rodents and iBAT in adult humans [27,28,49,60]. Nicotinic acid, a lipolysis inhibitor, substantially reverses this effect, indicating stored intracellular triglycerides provide much of the energy for oxidative metabolism in these tissues [49]. More recent studies have used a 3 compartment kinetic model with  $^{11}\text{C}$ -acetate  $K_2$  estimating  $\text{CO}_2$  production from the citric acid cycle [49,60], which may provide a better assessment of iBAT metabolic activity than other methods because it is sensitive to mobilization of intracellular energy stores. However, neither  $^{11}\text{C}$ -acetate  $K_{\text{mono}}$  or  $K_2$  have been compared to direct measurement of oxidative activity in adipose tissue.

### 3.5. Other Radiotracers

BAT is detected with other clinical and investigational radiotracers.  $^{123}\text{I}$ -metaiodobenzylguanidine (MIBG) SPECT/CT localizes sympathetic innervation by using a labeled norepinephrine analogue [75]. MIBG localizes BAT with similar sensitivity to FDG-PET/CT but is less temperature dependent [9,75,76]. The  $^{11}\text{C}$  PET tracer and norepinephrine analog  $^{11}\text{C}$ -meta-hydroxyephedrin has demonstrated sensitivity to BAT at thermoneutral conditions and its activity correlates with FDG uptake with acute cold in humans [77]. The commonly used SPECT/CT tracer  $^{99\text{m}}\text{Tc}$ -methoxyisobutylisonitrile (MIBI), which localizes to tissues with high mitochondrial density, detects BAT in a non-temperature dependent manner as shown in an example from our clinical practice (Figure 9) [76,78].  $^{15}\text{O}$ -labeled water PET/CT has been used in this setting to measure blood flow, which provides data to estimate tissue-specific metabolic rate using arterial oxygenation and known oxygen extraction fractions [77]. Din and colleagues combined  $^{15}\text{O}$ -labeled water PET/CT with inhaled  $^{15}\text{O}$  administration to directly measure tissue metabolic rate in humans [79]. The short (2 min) half-life of  $^{15}\text{O}$  allows for repeat PET scanning with another tracer on the same day [77,79]. Investigational radiotracer currently include the mitochondrial outer membrane translocator protein, visualized with  $^{18}\text{F}$ -FEPPA PET/CT and  $^{11}\text{C}$ -PBR28 PET/CT, the cannabinoid type 1 receptor, visualized with  $^{18}\text{F}$ -FMPEP-d2 PET/CT [80–83], and PD-L1, visualized with radiolabeled antibodies [84,85].

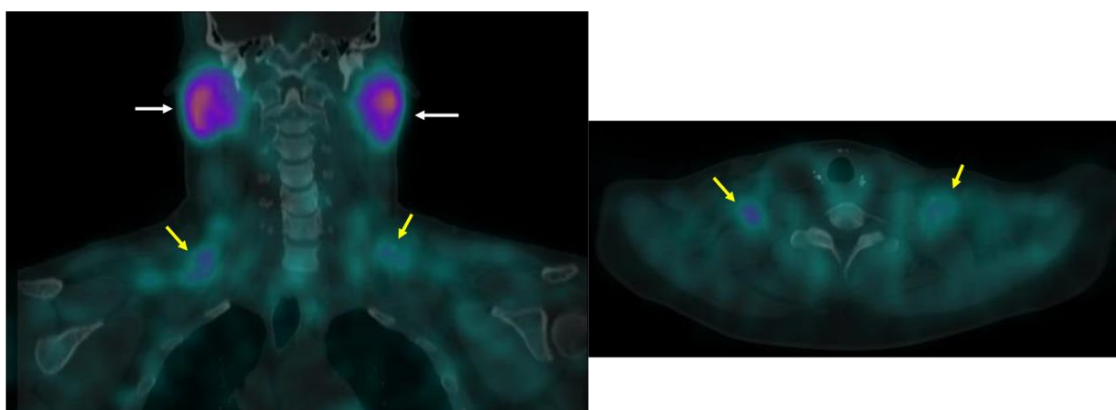


**Figure 9.**  $^{99m}\text{Tc}$ -MIBI uptake in iBAT on a clinical scan. Supraclavicular BAT uptake shown coronal and axial fused  $^{99m}\text{Tc}$ -MIBI-SPECT/CT (yellow arrows). Salivary gland uptake (white arrows) is normal.

#### 4. Emerging Technologies

BAT research invites application of novel imaging techniques. Inconsistent results from FDG-PET/CT studies limit our understanding of the tissue's relevance in human physiology and disease [86]. We briefly review 4 techniques that may assist future BAT research: xenon-enhanced imaging, hyperpolarized C-13 MRI, contrast-enhanced ultrasound, and optoacoustic imaging.

Xenon is a highly lipophilic gas transported in blood after inhalation. As BAT is more vascularized than WAT, xenon preferentially accumulates in BAT [87,88]. Branca and colleagues first utilized xenon as a substrate for hyperpolarized MRI, finding it was more sensitive to BAT presence in obese mice than FDG-PET/CT or MRI fat-fraction [87]. Next, they showed xenon-enhanced CT was more sensitive than FDG-PET/CT for BAT in mice and rhesus monkeys, and highly specific [88]. The authors importantly note FDG-PET/CT is most limited in obese subjects, the population of greatest interest in BAT research.

Carbon-13 produces a small magnetic field like hydrogen that can be utilized in MRI. However, its low isotopic abundance limits imaging without enrichment. Dissolution dynamic nuclear polarization (DNP) increases polarization of nuclear spins, greatly enhancing the generated magnetic field [89]. Commercial DNP systems now produce hyperpolarized  $^{13}\text{C}$  agents, most often pyruvate, for imaging studies. MRI obtained within about 1 min of hyperpolarized  $^{13}\text{C}$ -pyruvate injection show signal from downstream intermediates, notably lactate and bicarbonate, that indicate the rate of anaerobic (lactate) and aerobic (bicarbonate) metabolism in tissues [90]. The ratio of lactate/bicarbonate has been proposed as likely the most accurate metric generated in hyperpolarized  $^{13}\text{C}$ -pyruvate experiments as absolute values of  $^{13}\text{C}$ -lactate and  $^{13}\text{C}$ -bicarbonate are susceptible to effects of probe delivery and its membrane transport [90]. In a study by Lau and colleagues, hyperpolarized  $^{13}\text{C}$ -pyruvate MRI detected increased  $^{13}\text{C}$ -bicarbonate and  $^{13}\text{C}$ -lactate in BAT-associated interscapular regions of mice following norepinephrine stimulation [91]. Riis-Vestergaard then showed hyperpolarized  $^{13}\text{C}$ -pyruvate MRI of mice localizes BAT to the same regions as FDG-PET/MRI. The magnitude of increased metabolized pyruvate is similar to the magnitude of increased FDG uptake following cold stimulation, and there is increased anaerobic metabolism in BAT following cold stimulation (Figure 10) [92]. They also showed BAT increases metabolic activity independent of increased blood flow by adjusting for blood flow [92]. Advantages of this technique include lack of radiation and the ability to detect metabolic activity independent of blood flow. Disadvantages include limited availability, insensitivity to inactive BAT, and reliance on an upstream metabolic process.

Contrast-enhanced ultrasound (CEUS) with microbubbles estimates blood flow without radiation. It was first shown to detect BAT activation, as proven by histology, in mice [93]. Next, Flynn and colleagues showed it can detect increased blood flow with cooling in iBAT in human subjects with FDG-avid iBAT deposits [94]. CEUS application is limited by its reliance on iBAT activation and superficial field of view. However, the most important metabolically active fat pads in humans are

within CEUS's field of view and FDG-PET/CT is also limited by a reliance on iBAT activation. The major advantages of CEUS are its low cost and lack of radiation.

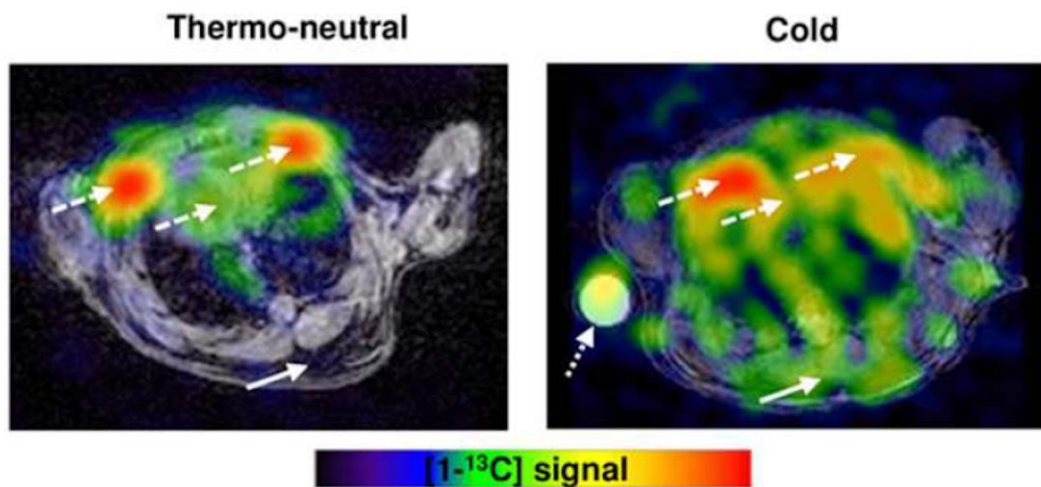


**Figure 10.** Hyperpolarized  $^{13}\text{C}$ -pyruvate MRI with cold exposure in a mouse. Hyperpolarized  $^{13}\text{C}$ -pyruvate MRI shows increased BAT activity in a mouse after cold exposure (solid arrow). The dashed arrows show the heart and large vessels and dotted arrow is a phantom. Image reproduced with permission from reference 92.

Multispectral optoacoustic tomography (MSOT) operates by pulsing light at a range of wavelengths for ultrashort periods of time triggering thermoelastic absorption by photoabsorbing molecules, which generates detectable mechanical waves at ultrasonic frequencies. MSOT arrays detect waves that can be reconstructed into images by unmixing known photoabsorption spectra of photoabsorbing biological molecules [95]. The Ntziachristos group recently showed MSOT can differentiate BAT from WAT *in vivo* and detect BAT activation by measuring real-time change in hemoglobin gradients in mice with a commercially available device (Figure 11) and in humans with a laboratory-modified handheld device [17]. Although wider use is limited by availability, the technology has the promise of a radiation-free, fast, and inexpensive means for repeatedly measuring iBAT activity in humans.

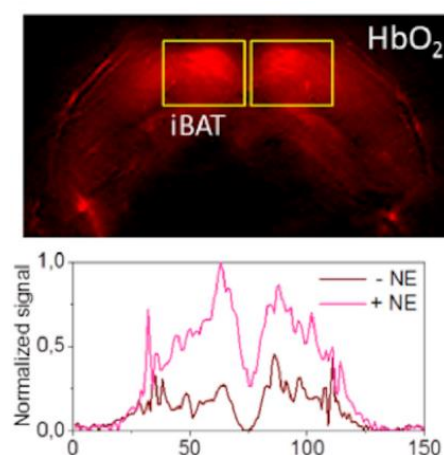


**Figure 11.** MSOT  $\text{HbO}_2$  map after norepinephrine treatment. MSOT image unmixed for  $\text{HbO}_2$  signal of murine interscapular BAT after treatment with norepinephrine (NE; top panel). BAT pads are shown in rectangles. The bottom panel shows the horizontal intensity profile with and without NE treatment. Image reproduced with permission from reference 95.

### 5. Summary

FDG-PET/CT is the de facto gold standard imaging study in BAT research. The relatively frequent presence of metabolically active fat depots in adult humans was first noted and the largest human studies in this field were gleaned from review of FDG-PET/CTs obtained for cancer surveillance and staging [51,52,56,96]. However, it is not prone to visualization of inactive BAT, probes a molecular event (glucose transport) upstream of BAT activity that is influenced by numerous other factors, it is expensive, and it involves radiation. However, advances in hardware and research protocols may allow for substantial radiation reduction in the near future [97]. Molecular imaging with other agents may improve sensitivity and specificity. Fatty acid probes, including <sup>18</sup>F-FTHA and <sup>123</sup>I-BMIPP, may detect BAT depots missed by FDG [30,49]. Dynamic imaging with <sup>11</sup>C-acetate provides information about oxidative metabolism and may therefore yield the useful data about BAT activity among molecular probes. Xenon-enhanced imaging appears may improve sensitivity in obese subjects [87,88]. Further advances in hyperpolarized MRI may allow more comprehensive evaluation of in vivo metabolism. Promising for repeated imaging of human subjects, contrast-enhanced ultrasound and multispectral optoacoustic tomography can detect iBAT activation without radiation [17,95]. Multispectral optoacoustic tomography can also differentiate BAT from WAT in the unstimulated state [17]. The physiological basis of key imaging modalities is summarized in Figure 12 and Table 1.

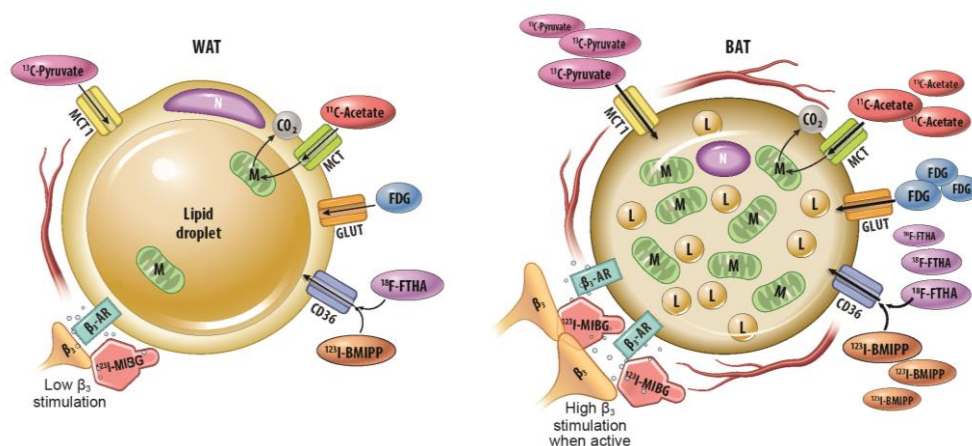


**Figure 12.** Physiological underpinnings of key imaging modalities for BAT research. The physiological basis for key imaging modalities in brown adipose tissue (BAT) research includes changes in inner action, vascularity, fat fraction, mitochondrial activity and key substrate transport and utilization. Comparison is made to white adipose tissue (WAT). N: nucleus, M: mitochondria, L: lipid droplet, FDG: <sup>18</sup>F-Fluorodeoxyglucose, FTHA: <sup>18</sup>F-Fluoro-6-Thia-Heptadecanoic Acid, BMIPP: <sup>123</sup>I-Beta-Methyl-Iodophenyl-Pentadecanoic Acid.

**Table 1.** Major differences between WAT and BAT on key imaging modalities. Comparison of WAT and BAT on key imaging modalities in BAT research. The relative finding of key factors are listed.

Modality	Feature	WAT Finding	BAT Finding	Radiation	References
CT	Density (HU)	↓	↑	+	16, 22, 25–28
MRI	Fat fraction	↓	↑	-	34, 36–39
MRI	Mitochondrial density (T2*/R2*)	↑	↓	-	37, 43, 44
FDG-PET/CT	SUV	↓	↑	++	13, 52–57
FTHA-PET/CT	Fractional uptake rate	↓	↑	++	28, 48, 59
BMIPP-SPECT/CT	Uptake	↓	↑	++	30
<sup>11</sup> C-Acetate-PET/CT	K <sub>mono</sub>	↓	↑	++	27, 28, 48, 59
<sup>11</sup> C-Acetate-PET/CT	K <sub>2</sub>	↓	↑	++	48, 59
Hyperpolarized <sup>13</sup> C MRI	Total signal	↓	↑	-	90, 91
Contrast-Enhanced Ultrasound	Blood flow	↓	↑	-	92-93

↓: decreased, ↑: increased, -: no ionizing radiation, +: ionizing radiation present, ++: more ionizing radiation present.

## 6. Conclusions

An ideal imaging study for human BAT research could detect BAT both when it is undergoing uncoupled mitochondrial oxidation and taking up fuel from the bloodstream and when it is not of high sensitivity. It could be repeated with limited or no radiation. Current methods typically require BAT induction with cooling to reach high levels of sensitivity. A reasonable humans-subjects research protocol for a BAT-activating intervention with current technologies is a screening FDG-PET/CT following a cooling protocol with a baseline radiation-free assessment (such as CEUS or MSOT where available) of identified depots' metabolic activity followed by sequential assessment of BAT activity. Further research may allow screening with more promising molecular studies with  $^{11}\text{C}$ -acetate or fatty acid tracers without the need for validation with FDG-PET/CT.

**Author Contributions:** Conceptualization, J.F. and O.K.Ö.; writing—original draft preparation, J.F.; writing—review and editing, O.K.Ö., A.S., P.E.S., D.J.C., and J.F.; visualization, J.F. and O.K.Ö.; supervision, O.K.Ö.; project administration, O.K.Ö.

**Funding:** O.K.O. receives support from the American Diabetes Association: I-17-ICTS-05.

**Acknowledgments:** We thank Erin Moore with the University of Texas Southwestern Radiology Illustration Services for assistance creating Figures 1 and 12 and Cathy Nakashima with the University of Texas Southwestern Medical Center Health Sciences Digital Library and Learning Center for assisting with the literature search.

**Conflicts of Interest:** The authors declare no conflict of interest.

## Abbreviations

BMI	Body mass index
PET	Positron emission tomography
BAT	Brown adipose tissue
iBAT	Inducible brown adipose tissue
MRI	Magnetic resonance imaging
WAT	White adipose tissue
CT	Computed tomography
HU	Hounsfield unit
NIH	National Institutes of Health
BARCIST	Brown Adipose Reporting Criteria in Imaging Studies
SUV	Standardized uptake values
FTHA	Fluoro-6-thia-heptadecanoic acid
BMIPP	Beta-methyl-iodophenyl-pentadecanoic acid
SPECT	Single-photon emission computed tomography
MIBG	Metaiodobenzylguanidine
MIBI	Methoxyisobutylisonitrile
DNP	Dissolution dynamic nuclear polarization
CEUS	Contrast-enhanced ultrasound
MSOT	Multispectral optoacoustic tomography

## References

1. Smith, K.B.; Smith, M.S. Obesity Statistics. *Prim. Care* **2016**, *43*, 121–135. [[CrossRef](#)]
2. Preston, S.H.; Vierboom, Y.C.; Stokes, A. The role of obesity in exceptionally slow US mortality improvement. *Proc. Natl. Acad. Sci. USA* **2018**, *115*, 957–961. [[CrossRef](#)]
3. Finkelstein, E.A.; Trogdon, J.G.; Cohen, J.W.; Dietz, W. Annual medical spending attributable to obesity: Payer- and service-specific estimates. *Health Aff. (Millwood)* **2009**, *28*, w822–w831. [[CrossRef](#)] [[PubMed](#)]
4. Apovian, C.M.; Aronne, L.J.; Bessesen, D.H.; McDonnell, M.E.; Murad, M.H.; Pagotto, U.; Ryan, D.H.; Still, C.D.; Endocrine, S. Pharmacological management of obesity: An endocrine Society clinical practice guideline. *J. Clin. Endocrinol. Metab.* **2015**, *100*, 342–362. [[CrossRef](#)] [[PubMed](#)]

5. Michael, D.J.; Donna, H.R.; Caroline, M.A.; Jamy, D.A.; Anthony, G.C.; Karen, A.D.; Frank, B.H.; Van, S.H.; John, M.J.; Robert, F.K.; et al. 2013 AHA/ACC/TOS Guideline for the Management of Overweight and Obesity in Adults. *Circulation* **2014**, *129* (Suppl. 2), S102–S138.
6. Khera, R.; Murad, M.H.; Chandar, A.K.; Dulai, P.S.; Wang, Z.; Prokop, L.J.; Loomba, R.; Camilleri, M.; Singh, S. Association of Pharmacological Treatments for Obesity With Weight Loss and Adverse Events: A Systematic Review and Meta-analysis. *JAMA* **2016**, *315*, 2424–2434. [[CrossRef](#)] [[PubMed](#)]
7. Lidell, M.E.; Betz, M.J.; Dahlqvist Leinhard, O.; Heglund, M.; Elander, L.; Slawik, M.; Mussack, T.; Nilsson, D.; Romu, T.; Nuutila, P.; et al. Evidence for two types of brown adipose tissue in humans. *Nat. Med.* **2013**, *19*, 631–634. [[CrossRef](#)] [[PubMed](#)]
8. Pope, M.; Budge, H.; Symonds, M.E. The developmental transition of ovine adipose tissue through early life. *Acta Physiol. (Oxf)* **2014**, *210*, 20–30. [[CrossRef](#)]
9. Bahler, L.; Deelen, J.W.; Hoekstra, J.B.; Holleman, F.; Verberne, H.J. Seasonal influence on stimulated BAT activity in prospective trials: A retrospective analysis of BAT visualized on 18F-FDG PET-CTs and 123I-mIBG SPECT-CTs. *J. Appl. Physiol.* **2016**, *120*, 1418–1423. [[CrossRef](#)]
10. Cypess, A.M.; Lehman, S.; Williams, G.; Tal, I.; Rodman, D.; Goldfine, A.B.; Kuo, F.C.; Palmer, E.L.; Tseng, Y.-H.; Doria, A.; et al. Identification and importance of brown adipose tissue in adult humans. *N. Engl. J. Med.* **2009**, *360*, 1509–1517. [[CrossRef](#)]
11. Cypess, A.M.; Weiner, L.S.; Roberts-Toler, C.; Franquet Elía, E.; Kessler, S.H.; Kahn, P.A.; English, J.; Chatman, K.; Trauger, S.A.; Doria, A.; et al. Activation of human brown adipose tissue by a  $\beta$ 3-adrenergic receptor agonist. *Cell Metab.* **2015**, *21*, 33–38. [[CrossRef](#)] [[PubMed](#)]
12. Wu, J.; Boström, P.; Sparks, L.M.; Ye, L.; Choi, J.H.; Giang, A.-H.; Khandekar, M.; Virtanen, K.A.; Nuutila, P.; Schaart, G.; et al. Beige Adipocytes Are a Distinct Type of Thermogenic Fat Cell in Mouse and Human. *Cell* **2012**, *150*, 366–376. [[CrossRef](#)] [[PubMed](#)]
13. Chen, K.Y.; Cypess, A.M.; Laughlin, M.R.; Haft, C.R.; Hu, H.H.; Bredella, M.A.; Enerbäck, S.; Kinahan, P.E.; Lichtenbelt, W.V.M.; Lin, F.I.; et al. Brown Adipose Reporting Criteria in Imaging Studies (BARCIST 1.0): Recommendations for Standardized FDG-PET/CT Experiments in Humans. *Cell Metab.* **2016**, *24*, 210–222. [[CrossRef](#)] [[PubMed](#)]
14. Ouellet, V.; Routhier-Labadie, A.; Bellemare, W.; Lakhali-Chaieb, L.; Turcotte, E.; Carpentier, A.C.; Richard, D. Outdoor temperature, age, sex, body mass index, and diabetic status determine the prevalence, mass, and glucose-uptake activity of 18F-FDG-detected BAT in humans. *J. Clin. Endocrinol. Metab.* **2011**, *96*, 192–199. [[CrossRef](#)] [[PubMed](#)]
15. Brendle, C.; Werner, M.K.; Schmadl, M.; la Fougère, C.; Nikolaou, K.; Stefan, N.; Pfannenberger, C. Correlation of Brown Adipose Tissue with Other Body Fat Compartments and Patient Characteristics: A Retrospective Analysis in a Large Patient Cohort Using PET/CT. *Acad. Radiol.* **2018**, *25*, 102–110. [[CrossRef](#)]
16. Prodhomme, H.; Ognard, J.; Robin, P.; Alavi, Z.; Salaun, P.-Y.; Ben Salem, D. Imaging and identification of brown adipose tissue on CT scan. *Clin. Physiol. Funct. Imaging* **2018**, *38*, 186–191. [[CrossRef](#)]
17. Reber, J.; Willershäuser, M.; Karlas, A.; Paul-Yuan, K.; Diot, G.; Franz, D.; Fromme, T.; Ovsepian, S.V.; Bézière, N.; Dubikovskaya, E.; et al. Non-invasive Measurement of Brown Fat Metabolism Based on Optoacoustic Imaging of Hemoglobin Gradients. *Cell Metab.* **2018**, *27*, 689–701.e4. [[CrossRef](#)]
18. Martinez-Tellez, B.; Nahon, K.J.; Sanchez-Delgado, G.; Abreu-Vieira, G.; Llamas-Elvira, J.M.; van Velden, F.H.P.; Pereira Arias-Bouda, L.M.; Rensen, P.C.N.; Boon, M.R.; Ruiz, J.R. The impact of using BARCIST 1.0 criteria on quantification of BAT volume and activity in three independent cohorts of adults. *Sci. Rep.* **2018**, *8*, 8567. [[CrossRef](#)]
19. Holstila, M.; Pesola, M.; Saari, T.; Koskensalo, K.; Raiko, J.; Borra, R.J.H.; Nuutila, P.; Parkkola, R.; Virtanen, K.A. MR signal-fat-fraction analysis and T2\* weighted imaging measure BAT reliably on humans without cold exposure. *Metab. Clin. Exp.* **2017**, *70*, 23–30. [[CrossRef](#)]
20. Deng, J.; Neff, L.M.; Rubert, N.C.; Zhang, B.; Shore, R.M.; Samet, J.D.; Nelson, P.C.; Landsberg, L. MRI characterization of brown adipose tissue under thermal challenges in normal weight, overweight, and obese young men. *J. Magn. Reson. Imaging* **2018**, *47*, 936–947. [[CrossRef](#)]
21. Jones, T.A.; Wayte, S.C.; Reddy, N.L.; Adesanya, O.; Dimitriadis, G.K.; Barber, T.M.; Hutchinson, C.E. Identification of an optimal threshold for detecting human brown adipose tissue using receiver operating characteristic analysis of IDEAL MRI fat fraction maps. *J. Magn. Reson. Imaging* **2018**, *51*, 61–68. [[CrossRef](#)] [[PubMed](#)]

22. Hsieh, J. *Computed Tomography: Principles, Design, Artifacts, and Recent Advances*, 3rd ed.; Society of Photo Optical: Bellingham, WA, USA, 2015; p. 639.
23. Blake, M.A.; Singh, A.; Setty, B.N.; Slattery, J.; Kalra, M.; Maher, M.M.; Sahani, D.V.; Fischman, A.J.; Mueller, P.R. Pearls and Pitfalls in Interpretation of Abdominal and Pelvic PET-CT. *Radiographics* **2006**, *26*, 1335–1353. [[CrossRef](#)] [[PubMed](#)]
24. Trattner, S.; Pearson, G.D.N.; Chin, C.; Cody, D.D.; Gupta, R.; Hess, C.P.; Kalra, M.K.; Kofler, J.M.; Krishnam, M.S.; Einstein, A.J. Standardization and optimization of CT protocols to achieve low dose. *J. Am. Coll. Radiol.* **2014**, *11*, 271–278. [[CrossRef](#)] [[PubMed](#)]
25. Reddy, N.L.; Jones, T.A.; Wayte, S.C.; Adesanya, O.; Sankar, S.; Yeo, Y.C.; Tripathi, G.; McTernan, P.G.; Randevara, H.S.; Kumar, S.; et al. Identification of Brown Adipose Tissue Using MR Imaging in a Human Adult With Histological and Immunohistochemical Confirmation. *J. Clin. Endocrinol. Metab.* **2014**, *99*, E117–E121. [[CrossRef](#)]
26. Baba, S.; Jacene, H.A.; Engles, J.M.; Honda, H.; Wahl, R.L. CT Hounsfield units of brown adipose tissue increase with activation: Preclinical and clinical studies. *J. Nucl. Med.* **2010**, *51*, 246–250. [[CrossRef](#)]
27. Blondin, D.P.; Labbé, S.M.; Tingelstad, H.C.; Noll, C.; Kunach, M.; Phoenix, S.; Guérin, B.; Turcotte, E.E.; Carpentier, A.C.; Richard, D.; et al. Increased brown adipose tissue oxidative capacity in cold-acclimated humans. *J. Clin. Endocrinol. Metab.* **2014**, *99*, E438–E446. [[CrossRef](#)]
28. Ouellet, V.; Labbé, S.M.; Blondin, D.P.; Phoenix, S.; Guérin, B.; Haman, F.; Turcotte, E.E.; Richard, D.; Carpentier, A.C. Brown adipose tissue oxidative metabolism contributes to energy expenditure during acute cold exposure in humans. *J. Clin. Investig.* **2012**, *122*, 545–552. [[CrossRef](#)]
29. Dadson, P.; Hannukainen, J.C.; Din, M.U.; Lahesmaa, M.; Kalliokoski, K.K.; Iozzo, P.; Pihlajamäki, J.; Karlsson, H.K.; Parkkola, R.; Salminen, P.; et al. Brown adipose tissue lipid metabolism in morbid obesity: Effect of bariatric surgery-induced weight loss. *Diabetes Obes. Metab.* **2018**, *20*, 1280–1288. [[CrossRef](#)]
30. Zhang, F.; Hao, G.; Shao, M.; Nham, K.; An, Y.; Wang, Q.; Zhu, Y.; Kusminski, C.M.; Hassan, G.; Gupta, R.K.; et al. An Adipose Tissue Atlas: An Image-Guided Identification of Human-like BAT and Beige Depots in Rodents. *Cell Metab.* **2018**, *27*, 252–262.e3. [[CrossRef](#)]
31. Bauwens, M.; Wierts, R.; van Royen, B.; Bucerius, J.; Backes, W.; Mottaghy, F.; Brans, B. Molecular imaging of brown adipose tissue in health and disease. *Eur. J. Nucl. Med. Mol. Imaging* **2014**, *41*, 776–791. [[CrossRef](#)]
32. Shimizu, I.; Aprahamian, T.; Kikuchi, R.; Shimizu, A.; Papanicolaou, K.N.; MacLauchlan, S.; Maruyama, S.; Walsh, K. Vascular rarefaction mediates whitening of brown fat in obesity. *J. Clin. Investig.* **2014**, *124*, 2099–2112. [[CrossRef](#)] [[PubMed](#)]
33. Pooley, R.A. Fundamental Physics of MR Imaging. *Radiographics* **2005**, *25*, 1087–1099. [[CrossRef](#)] [[PubMed](#)]
34. Stojanovska, J.; Lumeng, C.N.; Griffin, C.; Hernando, D.; Hoffmann, U.; Haft, J.W.; Kim, K.M.; Burant, C.F.; Singer, K.; Tsodikov, A.; et al. Water-fat magnetic resonance imaging quantifies relative proportions of brown and white adipose tissues: Ex-vivo experiments. *J. Med. Imaging (Bellingham)* **2018**, *5*, 024007. [[CrossRef](#)] [[PubMed](#)]
35. Romu, T.; Elander, L.; Leinhard, O.D.; Lidell, M.E.; Betz, M.J.; Persson, A.; Enerbäck, S.; Borga, M. Characterization of brown adipose tissue by water-fat separated magnetic resonance imaging. *J. Magn. Reson. Imaging* **2015**, *42*, 1639–1645. [[CrossRef](#)]
36. Franssens, B.T.; Eikendal, A.L.; Leiner, T.; van der Graaf, Y.; Visseren, F.L.J.; Hoogduin, J.M. Reliability and agreement of adipose tissue fat fraction measurements with water-fat MRI in patients with manifest cardiovascular disease. *NMR Biomed.* **2016**, *29*, 48–56. [[CrossRef](#)]
37. Lundström, E.; Strand, R.; Forslund, A.; Bergsten, P.; Weghuber, D.; Ahlström, H.; Kullberg, J. Automated segmentation of human cervical-supraclavicular adipose tissue in magnetic resonance images. *Sci. Rep.* **2017**, *7*, 3064. [[CrossRef](#)]
38. McCallister, A.; Zhang, L.; Burant, A.; Katz, L.; Branca, R.T. A pilot study on the correlation between fat fraction values and glucose uptake values in supraclavicular fat by simultaneous PET/MRI. *Magn. Reson. Med.* **2017**, *78*, 1922–1932. [[CrossRef](#)]
39. Stahl, V.; Maier, F.; Freitag, M.T.; Floca, R.O.; Berger, M.C.; Umatham, R.; Berriel Diaz, M.; Herzig, S.; Weber, M.-A.; Dimitrakopoulou-Strauss, A.; et al. In vivo assessment of cold stimulation effects on the fat fraction of brown adipose tissue using DIXON MRI. *J. Magn. Reson. Imaging* **2017**, *45*, 369–380. [[CrossRef](#)]

40. Koskensalo, K.; Raiko, J.; Saari, T.; Saunavaara, V.; Eskola, O.; Nuutila, P.; Saunavaara, J.; Parkkola, R.; Virtanen, K.A. Human Brown Adipose Tissue Temperature and Fat Fraction Are Related to Its Metabolic Activity. *J. Clin. Endocrinol. Metab.* **2017**, *102*, 1200–1207. [[CrossRef](#)]
41. Gifford, A.; Towse, T.F.; Walker, R.C.; Avison, M.J.; Welch, E.B. Characterizing active and inactive brown adipose tissue in adult humans using PET-CT and MR imaging. *Am. J. Physiol. Endocrinol. Metab.* **2016**, *311*, E95–E104. [[CrossRef](#)]
42. Franz, D.; Diefenbach, M.N.; Treibel, F.; Weidlich, D.; Syväri, J.; Ruschke, S.; Wu, M.; Holzapfel, C.; Drabsch, T.; Baum, T.; et al. Differentiating supraclavicular from gluteal adipose tissue based on simultaneous PDFF and T2\* mapping using a 20-echo gradient-echo acquisition. *J. Magn. Reson. Imaging* **2019**, *50*, 424–434. [[CrossRef](#)] [[PubMed](#)]
43. Wood, J.C.; Enriquez, C.; Ghugre, N.; Tyzka, J.M.; Carson, S.; Nelson, M.D.; Coates, T.D. MRI R2 and R2\* mapping accurately estimates hepatic iron concentration in transfusion-dependent thalassemia and sickle cell disease patients. *Blood* **2005**, *106*, 1460–1465. [[CrossRef](#)] [[PubMed](#)]
44. Kondur, A.K.; Li, T.; Vaitkevicius, P.; Afonso, L. Quantification of Myocardial Iron Overload by Cardiovascular Magnetic Resonance Imaging T2\* and Review of the Literature. *Clin. Cardiol.* **2009**, *32*, E54–E58. [[CrossRef](#)] [[PubMed](#)]
45. Zingaretti, M.C.; Crosta, F.; Vitali, A.; Guerrieri, M.; Frontini, A.; Cannon, B.; Nedergaard, J.; Cinti, S. The presence of UCP1 demonstrates that metabolically active adipose tissue in the neck of adult humans truly represents brown adipose tissue. *FASEB J.* **2009**, *23*, 3113–3120. [[CrossRef](#)]
46. Glover, G.H. Overview of Functional Magnetic Resonance Imaging. *Neurosurg. Clin. N. Am.* **2011**, *22*, 133–139. [[CrossRef](#)]
47. Chen, Y.-C.I.; Cypess, A.M.; Chen, Y.-C.; Palmer, M.; Kolodny, G.; Kahn, C.R.; Kwong, K.K. Measurement of human brown adipose tissue volume and activity using anatomic MR imaging and functional MR imaging. *J. Nucl. Med.* **2013**, *54*, 1584–1587. [[CrossRef](#)]
48. Kapoor, V.; McCook, B.M.; Torok, F.S. An Introduction to PET-CT Imaging. *Radiographics* **2004**, *24*, 523–543. [[CrossRef](#)]
49. Labbé, S.M.; Caron, A.; Bakan, I.; Laplante, M.; Carpentier, A.C.; Lecomte, R.; Richard, D. In vivo measurement of energy substrate contribution to cold-induced brown adipose tissue thermogenesis. *FASEB J.* **2015**, *29*, 2046–2058. [[CrossRef](#)]
50. Olsen, J.M.; Sato, M.; Dallner, O.S.; Sandström, A.L.; Pisani, D.F.; Chambard, J.C.; Amri, E.Z.; Hutchinson, D.S.; Bengtsson, T. Glucose uptake in brown fat cells is dependent on mTOR complex 2–promoted GLUT1 translocation. *J. Cell Biol.* **2014**, *207*, 365–374. [[CrossRef](#)]
51. Cohade, C.; Osman, M.; Pannu, H.K.; Wahl, R.L. Uptake in supraclavicular area fat (USA-Fat): Description on 18F-FDG PET/CT. *J. Nucl. Med.* **2003**, *44*, 170–176.
52. Hany, T.F.; Gharehpapagh, E.; Kamel, E.M.; Buck, A.; Himms-Hagen, J.; von Schulthess, G.K. Brown adipose tissue: A factor to consider in symmetrical tracer uptake in the neck and upper chest region. *Eur. J. Nucl. Med. Mol. Imaging* **2002**, *29*, 1393–1398. [[CrossRef](#)] [[PubMed](#)]
53. Lee, P.; Greenfield, J.R.; Ho, K.K.Y.; Fulham, M.J. A critical appraisal of the prevalence and metabolic significance of brown adipose tissue in adult humans. *Am. J. Physiol. Endocrinol. Metab.* **2010**, *299*, E601–E606. [[CrossRef](#)] [[PubMed](#)]
54. Blondin, D.P.; Labbé, S.M.; Turcotte, E.E.; Haman, F.; Richard, D.; Carpentier, A.C. A critical appraisal of brown adipose tissue metabolism in humans. *Clin. Lipidol.* **2015**, *10*, 259–280. [[CrossRef](#)]
55. Ong, F.J.; Ahmed, B.A.; Oreskovich, S.M.; Blondin, D.P.; Haq, T.; Konyer, N.B.; Noseworthy, M.D.; Haman, F.; Carpentier, A.C.; Morrison, K.M.; et al. Recent advances in the detection of brown adipose tissue in adult humans: A review. *Clin. Sci.* **2018**, *132*, 1039–1054. [[CrossRef](#)] [[PubMed](#)]
56. Steinberg, J.D.; Vogel, W.; Vejt, E. Factors influencing brown fat activation in FDG PET/CT: A retrospective analysis of 15,000+ cases. *Br. J. Radiol.* **2017**, *90*, 20170093. [[CrossRef](#)] [[PubMed](#)]
57. Bos, S.A.; Gill, C.M.; Martinez-Salazar, E.L.; Torriani, M.; Bredella, M.A. Preliminary investigation of brown adipose tissue assessed by PET/CT and cancer activity. *Skelet. Radiol.* **2018**, *48*, 413–419. [[CrossRef](#)]
58. Leitner, B.P.; Weiner, L.S.; Desir, M.; Kahn, P.A.; Selen, D.J.; Tsang, C.; Kolodny, G.M.; Cypess, A.M. Kinetics of human brown adipose tissue activation and deactivation. *Int. J. Obes. (Lond)* **2018**, *43*, 633–637. [[CrossRef](#)]

59. Pandey, M.K.; Bansal, A.; DeGrado, T.R. Fluorine-18 labeled thia fatty acids for PET imaging of fatty acid oxidation in heart and cancer. *Heart Metab.* **2011**, *51*, 15–19.
60. Labbé, S.M.; Caron, A.; Chechi, K.; Laplante, M.; Lecomte, R.; Richard, D. Metabolic activity of brown, “beige,” and white adipose tissues in response to chronic adrenergic stimulation in male mice. *Am. J. Physiol. Endocrinol. Metab.* **2016**, *311*, E260–E268. [[CrossRef](#)]
61. Fujiwara, S.; Takeishi, Y.; Atsumi, H.; Takahashi, K.; Tomoike, H. Fatty acid metabolic imaging with iodine-123-BMIPP for the diagnosis of coronary artery disease. *J. Nucl. Med.* **1997**, *38*, 175–180.
62. Biswas, S.K.; Sarai, M.; Hishida, H.; Ozaki, Y. 123I-BMIPP fatty acid analogue imaging is a novel diagnostic and prognostic approach following acute myocardial infarction. *Singap. Med. J.* **2009**, *50*, 943–948.
63. Yoshizumi, T.; Nozaki, S.; Fukuchi, K.; Yamasaki, K.; Fukuchi, T.; Maruyama, T.; Tomiyama, Y.; Yamashita, S.; Nishimura, T.; Matsuzawa, Y. Pharmacokinetics and metabolism of 123I-BMIPP fatty acid analog in healthy and CD36-deficient subjects. *J. Nucl. Med.* **2000**, *41*, 1134–1138. [[PubMed](#)]
64. Tamaki, N.; Yoshinaga, K. Novel iodinated tracers, MIBG and BMIPP, for nuclear cardiology. *J. Nucl. Cardiol.* **2011**, *18*, 135–143. [[CrossRef](#)] [[PubMed](#)]
65. Richmond, C.R.; Findlay, J.S. Half-life of iodine-125. *Health Phys.* **1966**, *12*, 865.
66. Lyssiotis, C.A.; Cantley, L.C. Acetate fuels the cancer engine. *Cell* **2014**, *159*, 1492–1494. [[CrossRef](#)]
67. Jeon, J.Y.; Lee, M.; Whang, S.H.; Kim, J.-W.; Cho, A.; Yun, M. Regulation of Acetate Utilization by Monocarboxylate Transporter 1 (MCT1) in Hepatocellular Carcinoma (HCC). *Oncol. Res.* **2018**, *26*, 71–81. [[CrossRef](#)]
68. Lewis, D.Y.; Boren, J.; Shaw, G.L.; Bielik, R.; Ramos-Montoya, A.; Larkin, T.J.; Martins, C.P.; Neal, D.E.; Soloviev, D.; Brindle, K.M. Late Imaging with [1-(11)C]Acetate Improves Detection of Tumor Fatty Acid Synthesis with PET. *J. Nucl. Med.* **2014**, *55*, 1144–1149. [[CrossRef](#)]
69. Toyoda, K.; Nakano, A.; Fujibayashi, Y.; Yonekura, Y.; Ueda, T.; Lee, J.-D. Diabetes mellitus impairs myocardial oxygen metabolism even in non-infarct-related areas in patients with acute myocardial infarction. *Int. J. Cardiol.* **2007**, *115*, 297–304. [[CrossRef](#)]
70. Hall, A.B.; Ziadi, M.C.; Leech, J.A.; Chen, S.-Y.; Burwash, I.G.; Renaud, J.; deKemp, R.A.; Haddad, H.; Mielniczuk, L.M.; Yoshinaga, K.; et al. Effects of short-term continuous positive airway pressure on myocardial sympathetic nerve function and energetics in patients with heart failure and obstructive sleep apnea: A randomized study. *Circulation* **2014**, *130*, 892–901. [[CrossRef](#)]
71. Regula, N.; Häggman, M.; Johansson, S.; Sörensen, J. Malignant lipogenesis defined by 11C-acetate PET/CT predicts prostate cancer-specific survival in patients with biochemical relapse after prostatectomy. *Eur. J. Nucl. Med. Mol. Imaging* **2016**, *43*, 2131–2138. [[CrossRef](#)]
72. Leisser, A.; Pruscha, K.; Ubl, P.; Wadsak, W.; Mayerhöfer, M.; Mitterhauser, M.; Hacker, M.; Kramer, G.; Shariat, S.; Karanikas, G.; et al. Evaluation of fatty acid synthase in prostate cancer recurrence: SUV of [(11)C]acetate PET as a prognostic marker. *Prostate* **2015**, *75*, 1760–1767. [[CrossRef](#)] [[PubMed](#)]
73. Grassi, I.; Nanni, C.; Allegri, V.; Morigi, J.J.; Montini, G.C.; Castellucci, P.; Fanti, S. The clinical use of PET with 11C-acetate. *Am. J. Nucl. Med. Mol. Imaging* **2011**, *2*, 33–47. [[PubMed](#)]
74. Labbe, S.M.; Caron, A.; Festuccia, W.T.; Lecomte, R.; Richard, D. Interscapular brown adipose tissue denervation does not promote the oxidative activity of inguinal white adipose tissue in male mice. *Am. J. Physiol. Endocrinol. Metab.* **2018**, *315*, E815–E824. [[CrossRef](#)] [[PubMed](#)]
75. Admiraal, W.M.; Holleman, F.; Bahler, L.; Soeters, M.R.; Hoekstra, J.B.; Verberne, H.J. Combining 123I-metaiodobenzylguanidine SPECT/CT and 18F-FDG PET/CT for the assessment of brown adipose tissue activity in humans during cold exposure. *J. Nucl. Med.* **2013**, *54*, 208–212. [[CrossRef](#)] [[PubMed](#)]
76. Baba, S.; Engles, J.M.; Huso, D.L.; Ishimori, T.; Wahl, R.L. Comparison of uptake of multiple clinical radiotracers into brown adipose tissue under cold-stimulated and nonstimulated conditions. *J. Nucl. Med.* **2007**, *48*, 1715–1723. [[CrossRef](#)] [[PubMed](#)]
77. Muzik, O.; Mangner, T.J.; Leonard, W.R.; Kumar, A.; Granneman, J.G. Sympathetic Innervation of Cold-Activated Brown and White Fat in Lean Young Adults. *J. Nucl. Med.* **2017**, *58*, 799–806. [[CrossRef](#)]
78. Cypess, A.M.; Doyle, A.N.; Sass, C.A.; Huang, T.L.; Mowschenson, P.M.; Rosen, H.N.; Tseng, Y.H.; Palmer, E.L., 3rd; Kolodny, G.M. Quantification of human and rodent brown adipose tissue function using 99mTc-methoxyisobutylisonitrile SPECT/CT and 18F-FDG PET/CT. *J. Nucl. Med.* **2013**, *54*, 1896–1901. [[CrossRef](#)]

79. u Din, M.; Raiko, J.; Saari, T.; Kudomi, N.; Tolvanen, T.; Oikonen, V.; Teuvo, J.; Sipila, H.T.; Savisto, N.; Parkkola, R.; et al. Human brown adipose tissue [(15)O]O<sub>2</sub> PET imaging in the presence and absence of cold stimulus. *Eur. J. Nucl. Med. Mol. Imaging* **2016**, *43*, 1878–1886. [[CrossRef](#)]
80. Lahesmaa, M.; Eriksson, O.; Gnad, T.; Oikonen, V.; Bucci, M.; Hirvonen, J.; Koskensalo, K.; Teuvo, J.; Niemi, T.; Taittonen, M.; et al. Cannabinoid Type 1 Receptors Are Upregulated During Acute Activation of Brown Adipose Tissue. *Diabetes* **2018**, *67*, 1226–1236. [[CrossRef](#)]
81. Eriksson, O.; Mikkola, K.; Espes, D.; Tuominen, L.; Virtanen, K.; Forsback, S.; Haaparanta-Solin, M.; Hietala, J.; Solin, O.; Nuutila, P. The Cannabinoid Receptor-1 Is an Imaging Biomarker of Brown Adipose Tissue. *J. Nucl. Med.* **2015**, *56*, 1937–1941. [[CrossRef](#)]
82. Hartimath, S.V.; Khanapur, S.; Boominathan, R.; Jiang, L.; Cheng, P.; Yong, F.F.; Tan, P.W.; Robins, E.G.; Goggi, J.L. Imaging adipose tissue browning using the TSPO-18kDa tracer [18F]FEPPA. *Mol. Metab.* **2019**, *25*, 154–158. [[CrossRef](#)] [[PubMed](#)]
83. Ran, C.; Albrecht, D.S.; Bredella, M.A.; Yang, J.; Liang, S.H.; Cypess, A.M.; Loggia, M.L.; Atassi, N.; Moore, A. PET Imaging of Human Brown Adipose Tissue with the TSPO Tracer [(11)C]PBR28. *Mol. Imaging Biol.* **2018**, *20*, 188–193. [[CrossRef](#)] [[PubMed](#)]
84. Hettich, M.; Braun, F.; Bartholoma, M.D.; Schirmbeck, R.; Niedermann, G. High-Resolution PET Imaging with Therapeutic Antibody-based PD-1/PD-L1 Checkpoint Tracers. *Theranostics* **2016**, *6*, 1629–1640. [[CrossRef](#)] [[PubMed](#)]
85. Ingram, J.R.; Dougan, M.; Rashidian, M.; Knoll, M.; Keliher, E.J.; Garrett, S.; Garforth, S.; Blomberg, O.S.; Espinosa, C.; Bhan, A.; et al. PD-L1 is an activation-independent marker of brown adipocytes. *Nat. Commun.* **2017**, *8*, 647. [[CrossRef](#)]
86. Sampath, S.C.; Sampath, S.C.; Bredella, M.A.; Cypess, A.M.; Torriani, M. Imaging of Brown Adipose Tissue: State of the Art. *Radiology* **2016**, *280*, 4–19. [[CrossRef](#)]
87. Branca, R.T.; He, T.; Zhang, L.; Floyd, C.S.; Freeman, M.; White, C.; Burant, A. Detection of brown adipose tissue and thermogenic activity in mice by hyperpolarized xenon MRI. *Proc. Natl. Acad. Sci. USA* **2014**, *111*, 18001–18006. [[CrossRef](#)]
88. Branca, R.T.; McCallister, A.; Yuan, H.; Aghajanian, A.; Faber, J.E.; Weimer, N.; Buchanan, R.; Floyd, C.S.; Antonacci, M.; Zhang, L.; et al. Accurate quantification of brown adipose tissue mass by xenon-enhanced computed tomography. *Proc. Natl. Acad. Sci. USA* **2018**, *115*, 174–179. [[CrossRef](#)]
89. Comment, A.; Merritt, M.E. Hyperpolarized magnetic resonance as a sensitive detector of metabolic function. *Biochemistry* **2014**, *53*, 7333–7357. [[CrossRef](#)]
90. Park, J.M.; Spielman, D.M.; Josan, S.; Jang, T.; Merchant, M.; Hurd, R.E.; Mayer, D.; Recht, L.D. Hyperpolarized (13)C-lactate to (13)C-bicarbonate ratio as a biomarker for monitoring the acute response of anti-vascular endothelial growth factor (anti-VEGF) treatment. *NMR Biomed.* **2016**, *29*, 650–659. [[CrossRef](#)]
91. Lau, A.Z.; Chen, A.P.; Gu, Y.; Ladouceur-Wodzak, M.; Nayak, K.S.; Cunningham, C.H. Noninvasive identification and assessment of functional brown adipose tissue in rodents using hyperpolarized <sup>13</sup>C imaging. *Int. J. Obes. (Lond)* **2014**, *38*, 126–131. [[CrossRef](#)]
92. Riis-Vestergaard, M.J.; Breining, P.; Pedersen, S.B.; Laustsen, C.; Stødkilde-Jørgensen, H.; Borghammer, P.; Jessen, N.; Richelsen, B. Evaluation of Active Brown Adipose Tissue by the Use of Hyperpolarized [1-13C]Pyruvate MRI in Mice. *Int. J. Mol. Sci.* **2018**, *19*, 9. [[CrossRef](#)] [[PubMed](#)]
93. Baron, D.M.; Clerte, M.; Brouckaert, P.; Raher, M.J.; Flynn, A.W.; Zhang, H.; Carter, E.A.; Picard, M.H.; Bloch, K.D.; Buys, E.S.; et al. In vivo noninvasive characterization of brown adipose tissue blood flow by contrast ultrasound in mice. *Circ. Cardiovasc. Imaging* **2012**, *5*, 652–659. [[CrossRef](#)] [[PubMed](#)]
94. Flynn, A.; Li, Q.; Panagia, M.; Abdelbaky, A.; MacNabb, M.; Samir, A.; Cypess, A.M.; Weyman, A.E.; Tawakol, A.; Scherrer-Crosbie, M. Contrast-Enhanced Ultrasound: A Novel Noninvasive, Nonionizing Method for the Detection of Brown Adipose Tissue in Humans. *J. Am. Soc. Echocardiogr.* **2015**, *28*, 1247–1254. [[CrossRef](#)] [[PubMed](#)]

95. Ntziachristos, V.; Razansky, D. Molecular Imaging by Means of Multispectral Optoacoustic Tomography (MSOT). *Chem. Rev.* **2010**, *110*, 2783–2794. [[CrossRef](#)]
96. Takx, R.A.P.; Ishai, A.; Truong, Q.A.; MacNabb, M.H.; Scherrer-Crosbie, M.; Tawakol, A. Supraclavicular Brown Adipose Tissue 18F-FDG Uptake and Cardiovascular Disease. *J. Nucl. Med.* **2016**, *57*, 1221–1225. [[CrossRef](#)]
97. Prieto, E.; Garcia-Velloso, M.J.; Rodriguez-Fraile, M.; Moran, V.; Garcia-Garcia, B.; Guillen, F.; Morales, M.I.; Sancho, L.; Penuelas, I.; Richter, J.A.; et al. Significant dose reduction is feasible in FDG PET/CT protocols without compromising diagnostic quality. *Phys. Med.* **2018**, *46*, 134–139. [[CrossRef](#)]



© 2019 by the authors. Licensee MDPI, Basel, Switzerland. This article is an open access article distributed under the terms and conditions of the Creative Commons Attribution (CC BY) license (<http://creativecommons.org/licenses/by/4.0/>).